Journal of Solid State Chemistry 182 (2009) 954–959

Contents lists available at ScienceDirect

Journal of Solid State Chemistry

journal homepage: www.elsevier.com/locate/jssc

Structural characterisation of the perovskite series $Sr_{0.9-x}Ca_xCe_{0.1}MnO_3$: Influence of the Jahn–Teller effect

Brendan J. Kennedy [a,*], Jimmy Ting [a], Qingdi Zhou [a], Zhaoming Zhang [b], Motohide Matsuda [c], Michihiro Miyake [c]

[a] School of Chemistry, The University of Sydney, New South Wales 2006, Australia
[b] Australian Nuclear Science and Technology Organisation, Private Mail Bag 1, Menai, NSW 2234, Australia
[c] Graduate School of Environmental Science, Okayama University, 3-1-1 Tsushima-Naka, Okayama 700-8530, Japan

ARTICLE INFO

Article history:
Received 15 September 2008
Received in revised form
21 November 2008
Accepted 9 December 2008
Available online 1 February 2009

Keywords:
Perovskite
Phase transition
Jahn–Teller effect

ABSTRACT

Fifteen perovskite-type compounds $Sr_{0.9-x}Ca_xCe_{0.1}MnO_3$, $x = 0$–0.9 in steps as fine as 0.05, have been synthesised by solid state methods, and the room temperature structures characterised using X-ray synchrotron powder diffraction. At low Ca contents ($x \leqslant 0.45$) the structures are tetragonal in space group *I*4/*mcm* and at high Ca contents ($x \geqslant 0.55$) the compounds are orthorhombic in space group *Pbnm*. At room temperature these two phases co-exist in the compound with $x = 0.5$. XANES measurements show the Ce to be present as Ce^{4+} in all the oxides. High temperature structures are reported for selected members.

1. Introduction

The cooperative Jahn–Teller (JT) effect remains an enigma in the solid state chemistry of Mn perovskites with some Mn^{3+} perovskites, such as $LaMnO_3$, exhibiting a large cooperative tetragonal distortion of the MnO_6 octahedra [1] yet others, such as Ca_2MnRuO_6, have regular MnO_6 octahedra [2]. The orbital ordering in the cooperative JT systems can have a profound impact on the magnetic and electrical properties of these perovskites. $LaMnO_3$ undergoes a structural phase transition at $T_{JT} \sim 750$ K, characterised by suppression of the cooperative JT distortions in the high temperature phase and an abrupt decrease in electrical resistivity [1]. The discovery of colossal magnetoresistance in mixed valence manganites $A_{1-x}R_xMnO_3$ (A = divalent alkaline earth cation; R = trivalent rare earth cation) has stimulated numerous studies that have revealed a large variety of magnetic arrangements and phase transitions that are not, as yet, well understood [3–5].

In 2000 Sundaresan and co-workers [6] reported an unusual sequence of structures in the series $Sr_{1-x}Ce_xMnO_3$ where increasing the amount of Mn^{3+} in the structure (by replacing Sr with Ce beyond $x = 0.1$) actually suppressed the JT effect. We have recently confirmed their observation that doping the cubic polytype of $SrMnO_3$ with Ce induces two first order phase transitions, initially to tetragonal in space group *I*4/*mcm* and then to orthorhombic in *Imma* [7]. The first of these, occurring at x just below 0.1, involves both long-range ordering of the JT elongated octahedra and cooperative tilting of the MnO_6 octahedra. The second transition, near $x = 0.35$, involves suppression of the cooperative JT distortions and re-orientation of the MnO_6 tilts. It may be that, like in Ca_2MnRuO_6 [2], large tilts are incompatible with a cooperative JT distortion. These Ce doped $SrMnO_3$ oxides are also of interest as a consequence of their unusual magnetic and electronic properties [8–10] and for their potential use in solid oxide fuel cells [11,12].

That the more heavily doped oxides have larger tilts can be rationalised by considering the size of the cations. Perovskites with a tolerance factor, $t = (r_A + r_O)/\sqrt{2}(r_B + r_O)$, less than one optimise their A–O and B–O bond lengths by cooperative tilting of the BO_6 octahedra. The further t is reduced the greater the tilt angle should be. Experimentally the magnitude of this tilting can be controlled by tuning the effective size of the A- and B-site cations, and there are now numerous examples of ABO_3 perovskites undergoing structural phase transitions as a function of temperature, pressure and composition [13–18]. Mn^{3+} is considerably larger than Mn^{4+} (0.645 vs 0.530 Å, respectively [19]), and so partially reducing Mn^{4+} in a perovskite might be expected to have a significant impact on the observed structure and this is evident in the series $Sr_{1-x}Ce_xMnO_3$.

The aim of the current work was to investigate the correlation between the tilting of the MnO_6 octahedra and the cooperative JT effect in some Ce doped manganites. We have exploited the well

* Corresponding author. Fax: +61 2 9351 3329.
E-mail address: B.Kennedy@chem.usyd.edu.au (B.J. Kennedy).

0022-4596/$ - see front matter © 2009 Elsevier Inc. All rights reserved.
doi:10.1016/j.jssc.2008.12.032

known compositional flexibility of perovskites to prepare solid solutions of the form $Sr_{0.9-x}Ca_xCe_{0.1}MnO_3$, and we report here structural studies of this series.

2. Experimental

About 4 g of each of the 15 compounds $Sr_{0.9-x}Ca_xCe_{0.1}MnO_3$, $x = 0$, 0.1, 0.15, 0.2, 0.25, 0.3, 0.35, 0.4, 0.45, 0.5, 0.55, 0.6, 0.7, 0.8 and 0.9 were prepared by solid-state reaction as follows. The appropriate stoichiometric amounts of pre-dried $SrCO_3$ (Kantou kagaku, 99.9%), $CaCO_3$ (Kantou kagaku, 99.9%), CeO_2 (Kantou kagaku, 99.99%) and Mn_3O_4 (Koujundo kagaku, 99.9%) were mixed for 24 h using a zirconia ball mill. The mixtures were then heated to 800 °C at 5 °/min and annealed at this temperature for 10 h in air. The calcined powders were cooled, reground in the ball mill for 24 h before being sintered at 1400 °C for 10 h in air and finally cooled at 5 °/min to room temperature. A selection of the samples was analysed using scanning electron microscopy (SEM) with an energy-dispersive spectrometer (EDS) to confirm the purity and homogeneity of the samples.

Room and variable temperature synchrotron X-ray powder diffraction patterns were collected on the high resolution Debye–Scherrer diffractometer at beamline 20B, the Australian National Beamline Facility, Photon Factory, Japan [20]. The wavelength was set at $\lambda = 0.80155$ Å (determined using NIST silicon Standard Reference Material 640c). The samples were finely ground and loaded into 0.3 mm capillaries that were continuously rotated during the measurements. Data were recorded using up to three BAS2000 Fuji image plates as detectors. Each image plate is 20×40 cm and each covers 40° in 2θ, allowing data to be collected over the range $2\theta = 5$–125° with a step size of 0.01005°. A thin strip ca. 0.5 cm wide is used to record each diffraction pattern. Variable temperature data were collected, using a custom-built furnace, at temperatures of up to 800 °C. For these measurements data were collected over the range $2\theta = 5$–85°. All measurements were performed under vacuum to minimise air scatter. Structural parameters were refined by the Rietveld method using the programme RIETICA [21]. A pseudo-Voigt function was used to model the peaks. The background was estimated by linear interpolation between regions where there were no Bragg peaks.

X-ray absorption near edge structure (XANES) measurements were performed on beamline 20B at the Photon Factory, KEK Japan, at the cerium L_3-edge (~5723 eV). The X-rays were selected using a channel cut Si(111) monochromator. Harmonic rejection was achieved by detuning the second crystal to 50% of the maximum X-ray intensity. Data were collected in transmission mode from samples diluted in BN and held in a 1 mm thick sample holder with Kapton windows. Dilution was required to prevent self-absorption. The XANES spectra were measured using three ion chambers, I_0 immediately before the sample and I_t immediately after the sample. Data were also measured simultaneously from a metal foil placed between the second and a third ionisation chamber (I_m) to provide an edge-shift calibration for the XANES data. The ion chambers were filled with appropriate quantities of inert Ar–He mixture gas.

3. Results

3.1. Ce XANES data

It is well-established that cerium L_3-edge XANES data are sensitive to the cerium oxidation state, with the near-edge regions of Ce^{3+} and Ce^{4+} being distinctly different [22,23]. The Ce^{3+} L_3-edge is characterised by a single intense resonance near 5723 eV. Ce^{4+} exhibits a distinct double peak in the immediate post-edge region; the first peak appears near 5726 eV and the peak-to-peak separation for $Ce^{4+}O_2$ is about 7.7 eV. The Ce L_3-edge XANES spectra for selected members of the series $Sr_{0.9-x}Ca_xCe_{0.1}MnO_3$ are shown in Fig. 1. From the appearance of these spectra and the edge position it can be deduced that the cerium in the samples is predominantly in oxidation state +4. Unfortunately the Mn K-edge overlaps with the Ce L_1-edge and so it was not possible to probe the oxidation state of the Mn in these samples using Mn K-edge XANES. Nevertheless, it is reasonable to expect charge balance is achieved by reduction of 20% of the Mn^{4+} to Mn^{3+} in these oxides, given that these samples appear not to contain any anion vacancies.

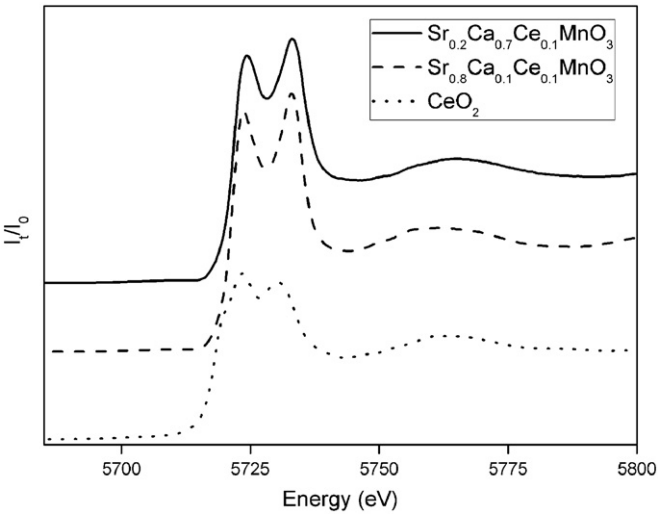

Fig. 1. Typical Ce L_3-edge XANES spectra obtained for members of the series $Sr_{0.9-x}Ca_xCe_{0.1}MnO_3$. The shape of the spectra and the chemical shift are well matched to that of CeO_2. The spectrum for CeO_2 collected under identical conditions is also illustrated.

3.2. Room temperature diffraction studies

The structures were identified from both the splitting of the main peaks and the presence or otherwise of the weak superlattice peaks associated with the different octahedral tilt patterns. The $x = 0.8$ and 0.9 compounds were, like $CaMnO_3$ itself [24], clearly orthorhombic. The main peaks showed, in Figs. 2 and 3, complex splitting, and superlattice reflections from *R*-point, *M*-point and *X*-point distortions were all observed in the patterns. The appropriate space group is *Pbnm* and the tilt system is described in Glazer's notation as $a^-a^-c^+$ [25]. Ganguly et al. reached the same conclusion for $Ca_{0.9}Ce_{0.1}MnO_3$ using a combination of electron and powder X-ray diffraction [26]. At $x = 0.7$ the splitting of the 222 line (indexed on the cubic perovskite subcell) near $2\theta = 43.1°$ ($d = 1.10$ Å) is absent, yet the strongest *R*-, *M*- and *X*-point reflections are clearly evident in the diffraction patterns. The occurrence of pseudo-cubic, but strictly, orthorhombic phases in perovskites has been noted previously [15,17,27]. We conclude that the pseudo-cubic structures with $0.55 \leqslant x \leqslant 0.70$ are also orthorhombic with space group *Pbnm*.

At compositions from $x = 0$ up to $x = 0.45$, the *h* 0 0 peaks were split but there was no splitting of the *h h h* peaks (when indexed on the cubic perovskite subcell). Superlattice reflections due to *R*-point distortions were clearly evident throughout this composition range, but none attributable to *M*- or *X*-point distortions were observed. This is consistent with a tetragonal structure in space group *I*4/*mcm*. These results are very similar to those

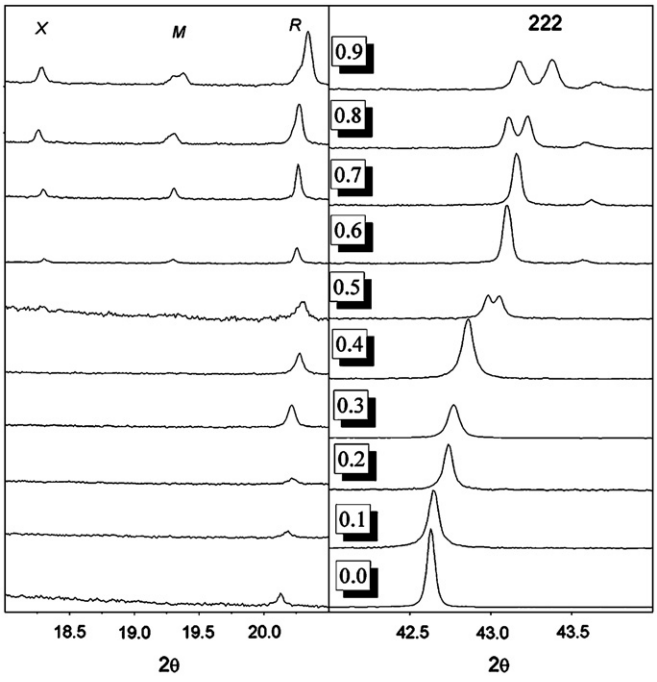

Fig. 2. Portion of the diffraction profiles for $Sr_{0.9-x}Ca_xCe_{0.1}MnO_3$. The splitting of the 2 2 2 reflection near $2\theta = 43^\circ$ is apparent at high Ca contents $x \geqslant 0.80$, yet *M* and *X*-point reflections persist to $x = 0.60$. *R*-point superlattice reflections indicative of out-of-phase tilts are observed, in all the patterns, near $2\theta = 20.2^\circ$. The numbers refer to the Ca content in each sample.

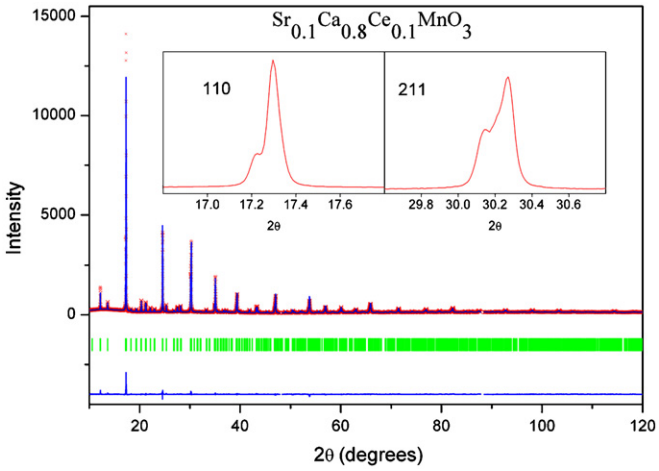

Fig. 3. Observed, calculated and difference X-ray diffraction pattern for $Sr_{0.1}Ca_{0.8}Ce_{0.1}MnO_3$ at room temperature. The insets show the splitting of the (cubic) 1 1 0 and 2 1 1 reflections near $2\theta = 17.3$ and 30.2°, respectively, indicative of orthorhombic symmetry.

reported by Martin and co-workers for the closely related $Sr_{0.9-x}Ca_xSm_{0.1}MnO_3$ system [28], although unlike these authors we did not observe an hexagonal phase at high Sr contents.

The patterns were then analysed by the Rietveld method, using the programme RIETICA, assuming the structures indicated above. In *Pbnm* the *A* type cations (Sr, Ca and Ce) are on the 4*c* site at $x\,y\,\frac{1}{4}$, the Mn cations on the 4*a* sites at 0 0 0, O1 on the 4*c* sites at $x\,y\,\frac{1}{4}$, and O2 on the 8*d* sites at $x\,y\,z$. In *I*4/*mcm* the *A* cations are on 4*b* sites at $0\,\frac{1}{2}\,\frac{1}{4}$, the Mn cations on the 4*c* sites at 0 0 0, the O1 on the 4*a* sites $0\,0\,\frac{1}{4}$, and O2 on the 8*h* sites at $\frac{1}{4}-\delta\ \frac{1}{4}+\delta 0$. The atomic co-ordinates obtained for the $x = 0.9$ sample were in reasonable agreement with those reported from neutron diffraction studies

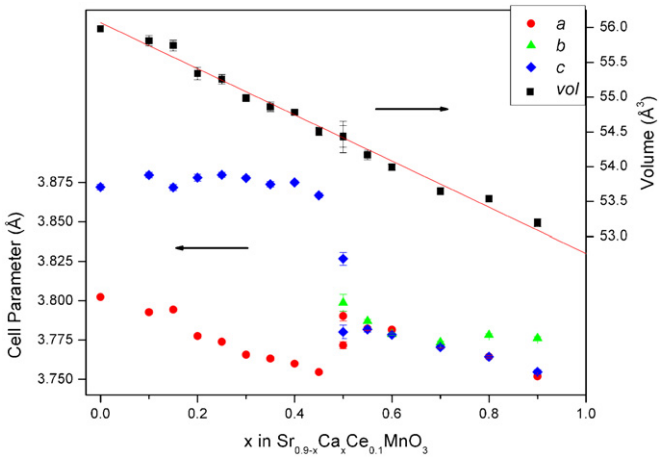

Fig. 4. Variation of the reduced lattice parameters and the subcell volume with composition in $Sr_{0.9-x}Ca_xCe_{0.1}MnO_3$. For $x \leqslant 0.45$ the structures are in *I*4/*mcm*, for $x = 0.5$ the structure is a mixture of *I*4/*mcm* and *Pbnm* and for $x \geqslant 0.55$ the structures are in *Pbnm*.

for $CaMnO_3$ [29], and co-ordinates obtained in the other refinements were typical for the structures assumed (see Table 1). The composition dependence of the lattice parameters obtained from the Rietveld refinements is illustrated in Fig. 4. We note that in the tetragonal structures anisotropic broadening of the Bragg reflections indicative of local strains are evident in the diffraction patterns. Such broadening is not evident in the orthorhombic materials.

The diffraction pattern for the sample with $x = 0.5$ was not well fitted in either of the above models, but was well fitted as a mixture of two phases, one in *Pbnm* and the other in *I*4/*mcm*. The refined Ca:Sr ratio in each of the two phases was within one esd of each other, indicating that the formation of the two phases is not related to preferential segregation of the Ca and Sr cations. Since refining the Ca:Sr ratio did not lead to a noticeable improvement in the quality of the fit, these were fixed at their nominal values in the final refinements. Due to the fact that the data were collected at a single wavelength, it was not feasible to confirm if the Ce was equally distributed over the two phases, except that SEM/EDS analysis showed the sample to be homogeneous. Recall that a perovskite cannot transform continuously from *Pbnm* to *I*4/*mcm* and that a first order step must be involved [30]. The co-existence of these two phases is indicative of a first order phase transition and was also observed in the series $Sr_{1-x}Ca_xMnO_3$ at $x \sim 0.5$ [31]. This co-existence demonstrates the absence of the *Imma* phase observed at higher Ce doping in $Sr_{1-x}Ce_xMnO_3$ [6] and is a significant difference between the two series. The *Imma* phase was observed over a small composition range in the series $Pr_{0.5}Sr_{0.5-x}Ca_xMnO_3$ [32], but was not observed in the series $Sr_{0.9-x}Ca_xSm_{0.1}MnO_3$ [28].

The tilt angle in the tetragonal samples was estimated from the refined oxygen positional parameters using $\tan\varphi = 1-4x(O2)$ [33]. The tilt angle, φ, shows a systematic increase with increasing Ca content, from around 3.9° in $Sr_{0.9}Ce_{0.1}MnO_3$ to 7.5° in $Sr_{0.4}Ca_{0.5}Ce_{0.1}MnO_3$ reflecting the evolution in the tolerance factor. Despite this progressive increase in φ, the tetragonal elongation of the MnO_6 octahedra remains essentially unchanged with the two axial bond distances being around 0.04 Å longer than the four equatorial Mn–O distances in all the tetragonal samples.

The distortion of the MnO_6 octahedra can be quantified using the quantity $\Delta d = (1/6)\sum[(d_n - d)/d]^2$ where d is the mean Mn–O distance and d_n the individual Mn–O distance [1]. The discontinuity in the lattice parameters observed near $x = 0.5$ in Fig. 4

Table 1
Room temperature crystallographic parameters for $Ca_{0.9}Ce_{0.1}MnO_3$ and $Sr_{0.6}Ca_{0.3}Ce_{0.1}MnO_3$.

Space group	$Ca_{0.9}Ce_{0.1}MnO_3$ *Pbnm* (orthorhombic)	$Sr_{0.6}Ca_{0.3}Ce_{0.1}MnO_3$ *I4/mcm* (tetragonal)
a (Å)	5.30579 (8)	5.32528 (8)
b (Å)	5.34034 (9)	
c (Å)	7.50927 (14)	7.75581 (13)
V (Å^3)	212.773 (6)	219.944 (4)
Mn		
B (Å^2)	0.28 (12)	0.42 (2)
Ca, Sr, Ce		
x	0.0034 (5)	0
y	0.5341 (1)	0.5
B (Å^2)	0.99 (15)	0.89 (3)
O1		
x	−0.0695 (9)	0
y	−0.0152 (7)	0
B (Å^2)	0.66 (3)	0.42 (2)
O2		
x	0.2097 (6)	0.2187 (5)
y	0.2887 (5)	0.2813 (5)
z	0.0369 (5)	0
B (Å^2)	0.66 (3)	0.24 (4)
R_p, R_{wp} (%)	4.67, 4.86	8.03, 6.64
Mn–O(1) (Å)	1.9149 (10)	1.9390 (1)
Mn–O(2) (Å)	1.9215 (29)	1.8974 (4)
Mn–O(2) (Å)	1.9292 (30)	

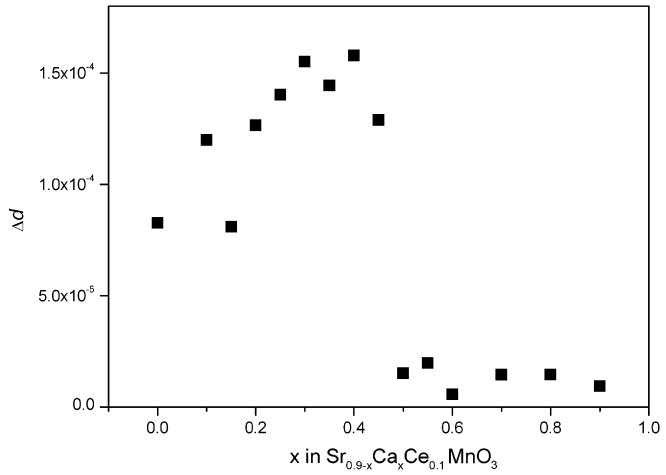

Fig. 5. Composition dependence of the distortion parameter defined as $\Delta d = (1/6)\sum[(d_n - d)/d]^2$ in the series $Sr_{0.9-x}Ca_xCe_{0.1}O_3$.

corresponds to a marked reduction in the distortion of the MnO_6 octahedra (Δd) from $\sim 15 \times 10^{-5}$ for $x < 0.50$ to $\sim 1.5 \times 10^{-5}$ for $x > 0.50$, illustrated in Fig. 5. The abrupt reduction in Δd near $x = 0.5$ is a consequence of a first order transition from the JT distorted tetragonal structure to the orthorhombic structure, where the cooperative JT effect seems to be absent. There is no obvious volume discontinuity accompanying the composition-induced phase transition.

3.3. Variable temperature diffraction studies

The temperature dependence of the structures of a number of samples was investigated at temperatures up to 800 °C. The structure of $Sr_{0.55}Ca_{0.35}Ce_{0.1}MnO_3$ is tetragonal in *I4/mcm* at room temperature and the patterns recorded at or below 550 °C were well fitted by this choice of space group. At higher temperatures we found no evidence for either splitting of the Bragg reflections or the presence of any *R*-point superlattice reflections. Satisfactory

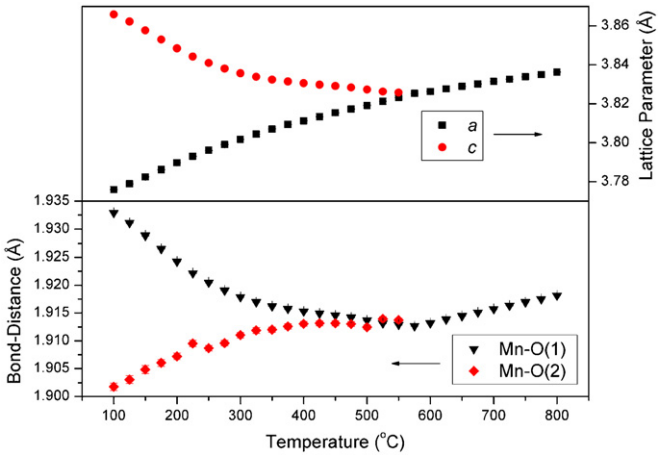

Fig. 6. The temperature dependence of the Mn–O bond distances and reduced lattice parameters for $Sr_{0.55}Ca_{0.35}Ce_{0.1}MnO_3$.

fits could be obtained using a cubic structure in $Pm\bar{3}m$. These results are summarised in Fig. 6 and are similar to the results we recently reported for $Sr_{0.9}Ce_{0.1}MnO_3$ where a continuous $I4/mcm$–$Pm\bar{3}m$ transition occurred near 215 °C [7]. As has been previously reported for Sr_2SbMnO_6 [34] and $SrRu_{0.5}Mn_{0.5}O_3$ [35] the transition to the cubic structure was accompanied by loss of the large tetragonal distortion of the MnO_6 octahedra, as is also illustrated in Fig. 6. Of note in this figure is the apparent change in the rate of contraction of the *c*-axis near 300 °C. At around the same temperature the elongation of the MnO_6 is observed to become reasonably small. This suggests the possibility of a transition related to the removal of the cooperative JT ordering at $T \sim 300$ °C. The small distortion of the MnO_6 octahedra observed at 300 °C $< T <$ 550 °C could be a result of octahedral tilting as it can induce a small elongation of the octahedra even in the absence of a cooperative JT distortion, and this has been observed in the high temperature tetragonal phase of $CaTiO_3$ [33].

The $Pm\bar{3}m - I4/mcm$ transition involves the condensation of the R_{25} soft mode at the *R*-point on the Brillouin zone boundary [36]. This mode is associated with the rotation of MnO_6 octahedra around the [001] axis, $a^0a^0c^-$ in Glazer's notation [25]. The rotation angle, φ, of these octahedra is therefore the primary order parameter *Q* of the transition. The magnitude of the tilts in the tetragonal phase was estimated from the refined atomic coordinates, and as demonstrated in Fig. 7, it is possible to reproduce its variation with temperature by the expression $\varphi \propto (T_C - T)^{1/4}$, where T_C is the transition temperature to the cubic phase. This behaviour, which was also seen in $SrZrO_3$ [37] and $CaTiO_3$ [33], is typical of a tricritical phase transition. The nature of the tetragonal to cubic phase transition in $Sr_{0.55}Ca_{0.35}Ce_{0.1}MnO_3$ was also investigated by the examination of the spontaneous tetragonal strain calculated from the lattice parameters as $\varepsilon_t = (c_t - \sqrt{2}a_t)/\sqrt{3}a_0$ where a_t and c_t are the observed tetragonal lattice parameters and a_0 is the equivalent (strain free) cubic lattice parameter estimated by extrapolation from the cubic region. The temperature dependence of the tetragonal strain is also shown in Fig. 7, illustrating two distinct linear regions, namely below 300 °C and above. This suggests that the strain at $T < 300$ °C consists of two components due to the co-operative JT distortion and octahedral tilting, respectively. This confirms the postulation that there are two transitions occurring, the first due to the quenching of the JT distortion and the second the removal of the octahedral tilts.

The structure of $Sr_{0.4}Ca_{0.5}Ce_{0.1}MnO_3$ was also investigated as a function of temperature. A feature of these variable temperature results is the extensive two-phase (*Pbnm* and *I4/mcm*) region

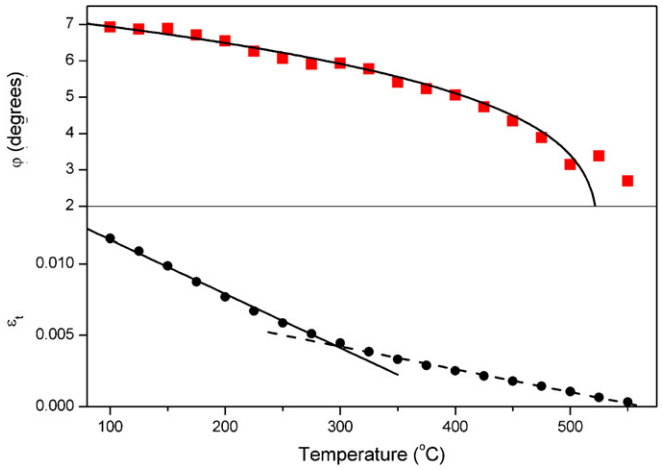

Fig. 7. (Upper panel) The temperature dependence of the MnO_6 tilt angle for $Sr_{0.55}Ca_{0.35}Ce_{0.1}MnO_3$. The solid line is the best fit to the expression $\varphi = K(T_C - T)^{1/4}$. The scatter at high temperature reflects the weakness of the *R*-point superlattice reflections in the X-ray diffraction patterns close to the transition point. (Lower panel) Temperature dependence of the spontaneous tetragonal strain in $Sr_{0.55}Ca_{0.35}Ce_{0.1}MnO_3$, illustrating the transition near 300 °C.

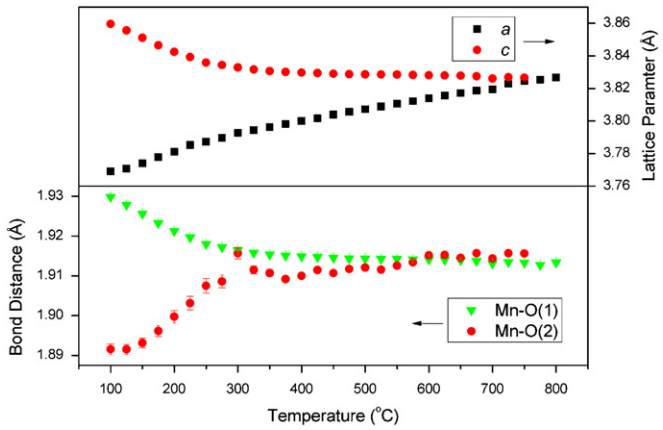

Fig. 8. The temperature dependence of the Mn–O bond distances and reduced lattice parameters of the tetragonal and cubic phases for $Sr_{0.4}Ca_{0.5}Ce_{0.1}MnO_3$.

indicative of a first order phase transition. Such behaviour is not expected to occur for a continuous phase transition and is taken as strong evidence against the involvement of an intermediate *Imma* phase in the transition. A consequence of the co-existence of the *Pbnm* and *I*4/*mcm* phases is the lower than usual accuracy in the refined values of the oxygen positional parameters, especially where the amount of the second phase present is relatively small. Nevertheless, we obtained satisfactory refinements and observed a greater distortion of the MnO_6 octahedra in the tetragonal phase than in the orthorhombic phase.

Since the orthorhombic phase in $Sr_{0.4}Ca_{0.5}Ce_{0.1}MnO_3$ is the minor phase in the patterns recorded below 425 °C, it is believed that the behaviour of the tetragonal (major) phase is not affected by the presence of the second phase. The diffraction data offer no evidence for this persistence of the orthorhombic phase in the patterns recorded at or above 450 °C. Fig. 8 shows the temperature dependence of the reduced lattice parameters and bond distances of the tetragonal and cubic phases for $Sr_{0.4}Ca_{0.5}Ce_{0.1}MnO_3$. As found in $Sr_{0.55}Ca_{0.35}Ce_{0.1}MnO_3$ we find evidence for two phase transitions. Initially there is an apparent change in the rate of contraction of the *c*-axis near 300 °C that is accompanied by a large reduction in the tetragonal distortion of the MnO_6 octahedra

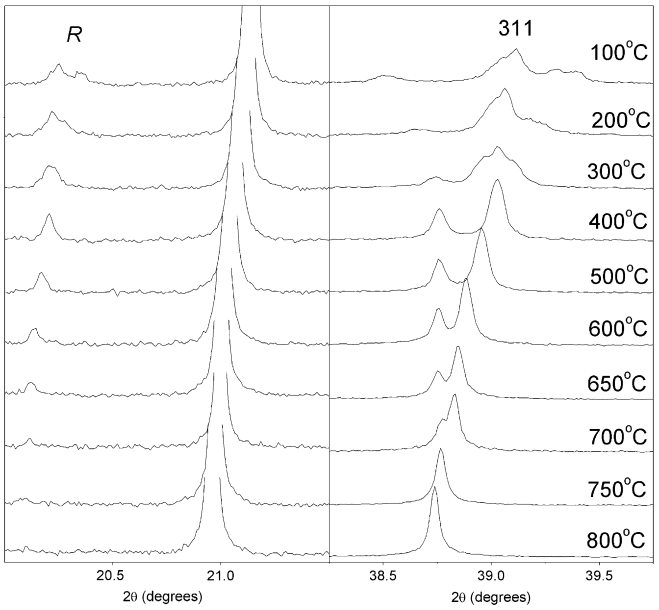

Fig. 9. Portions of the diffraction patterns for $Sr_{0.4}Ca_{0.5}Ce_{0.1}MnO_3$ illustrating the changes accompanying the transitions from orthorhombic to tetragonal, and then to cubic. The left hand side panel highlights the persistence of the weak *R*-point reflection near $2\theta = 20.3°$ to near 750 °C. Note the complexity of the profile near $2\theta = 39°$ (corresponding to the cubic 311 reflection) in the pattern recorded at 300 °C is due to the co-existence of the *Pbnm* and *I*4/*mcm* phases. This reflection becomes a singlet near 750 °C at the transition to cubic.

(Fig. 8). Above ~300 °C the MnO_6 octahedron is relatively undistorted, yet the *R*-point reflections and the tetragonal distortion of the cell persist to near 750 °C, Fig. 9. The two transitions are very obvious from the temperature dependence of the tetragonal strain as illustrated in Fig. 10. The lower than usual precision of the refinements in the two-phase region, noted above, precluded us from establishing reliable temperature dependence of the octahedral tilt angle.

Comparison of the results in Figs. 6 and 8 demonstrates that the first transition occurs at around the same temperature in the two samples with $x \sim 0.35$ and 0.5, yet the transition to cubic occurs at a much higher temperature in the Ca richer $x = 0.5$ sample. The smaller ionic radii of Ca^{2+} cf. Sr^{2+} [19] is expected to increase the magnitude of the octahedral tilting in the $x = 0.5$ sample and consequently the temperature at which it transforms to cubic, as observed. Since the two samples contain the same amount of the JT active Mn^{3+} cation, it is reasonable to anticipate that the loss of the cooperative JT ordering should occur at the same temperature, demonstrating that the transition near 300 °C is a consequence of the JT effect.

A further point of interest from these studies is that throughout the two phase region in $Sr_{0.4}Ca_{0.5}Ce_{0.1}MnO_3$ the volume of the orthorhombic phase is smaller than that of the tetragonal phase, see Fig. 11. This observation is similar to that made by Chatterji et al. [1] on $LaMnO_3$ where the cooperative JT ordering results in an apparent increase in volume of the unit cell, although the present results suggest the JT effect is only present in the tetragonal phase. This is worthy of further study.

Finally we also examined the temperature dependence of the structure of $Sr_{0.3}Ca_{0.6}Ce_{0.1}MnO_3$ from 100 to 800 °C. The structure remains orthorhombic in *Pbnm* until near 700 °C at which point it undergoes an, apparently, first order transition to the tetragonal *I*4/*mcm* structure. The diffraction pattern at 800 °C was clearly tetragonal with $a = 5.3889(1)$ and $c = 7.6461(1)$ Å; however, the two independent Mn–O bond distances were essentially identical

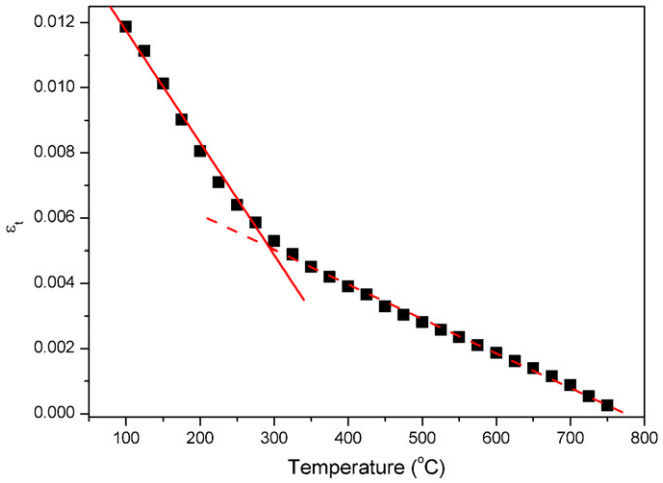

Fig. 10. Temperature dependence of the spontaneous tetragonal strain in $Sr_{0.4}Ca_{0.5}Ce_{0.1}MnO_3$.

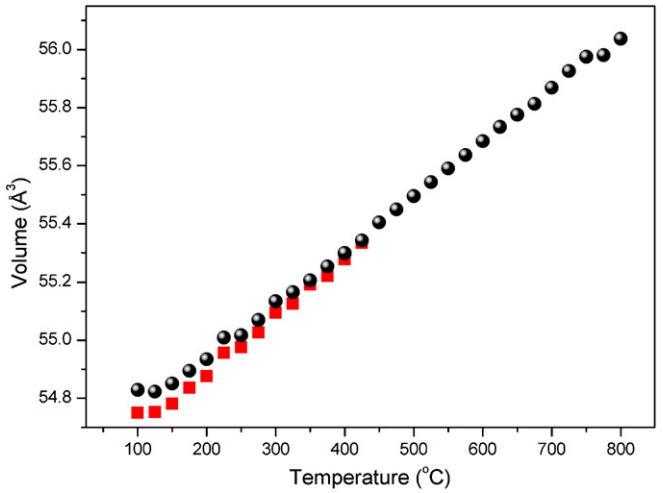

Fig. 11. Temperature dependence of the equivalent cubic perovskite subcell volumes for the tetragonal (circles) and orthorhombic (squares) phases in $Sr_{0.4}Ca_{0.5}Ce_{0.1}MnO_3$. Above 450 °C the structure is (single phase) tetragonal and above 750 °C it is cubic (circles).

viz. Mn–O(1) = 1.9115(10) Å and Mn–O(2) = 1.9139(34) Å demonstrating the absence of a cooperative JT distortion at this temperature. Still higher temperatures would be required to observe the expected transition to the cubic structure for this composition.

In summary, we have investigated the structural sequence in the series $Sr_{0.9-x}Ca_xCe_{0.1}MnO_3$. We find at room temperature the Ca rich samples have an orthorhombic structure in *Pbnm* that is characterised by relatively regular MnO_6 octahedra indicating the absence of a static JT effect. The Sr rich samples have a tetragonal structure in *I*4/*mcm* with the MnO_6 octahedra exhibiting a noticeable elongation due to orbital ordering. Temperature dependent studies of two samples with $x = 0.35$ and 0.5 reveal a continuous transition to cubic occurring in both samples. The transformation to cubic symmetry apparently involves two distinct transitions; the first is due to the removal of the orbital ordering and the second loss of the octahedral tilting. The temperature at which the first of these transitions occurs appears to be insensitive to the Ca:Sr ratio whereas the transition temperature for the second of these increases noticeably with increasing Ca (and decreasing Sr) content. Studies of additional systems likely to show the same effect are clearly warranted.

Acknowledgments

This work was, in part, performed at the Australian National Beamline Facility with support from the Australian Synchrotron Research Program, which is funded by the Commonwealth of Australia under the Major National Research Facilities programme. B.J.K. acknowledges the support of the Australian Research Council.

References

[1] T. Chatterji, F. Fauth, B. Ouladdiaf, P. Mandal, B. Ghosh, Physical Review B 68 (2003) 052406.
[2] M.W. Lufaso, P.M. Woodward, J. Goldberger, Journal of Solid State Chemistry 177 (2004) 1651.
[3] S. Jin, T.H. Tiefel, M. McCormack, R.A. Fastnacht, R. Ramesh, L.H. Chen, Science 264 (1994) 413.
[4] A. Maignan, C. Martin, F. Damay, B. Raveau, Chemistry of Materials 10 (1998) 950.
[5] Z. Zeng, M. Greenblatt, M. Croft, Physical Review B 63 (2001) 224410.
[6] A. Sundaresan, J.L. Tholence, A. Maignan, C. Martin, M. Hervieu, B. Raveau, E. Suard, European Physical Journal B 14 (2000) 431.
[7] B.J. Kennedy, P.J. Saines, Q. Zhou, Z. Zhang, M. Matsuda, M. Miyake, Journal of Solid State Chemistry 181 (2008) 2639.
[8] W.J. Lu, Y.P. Sun, X.B. Zhu, W.H. Song, J.J. Du, Physics Letters A 349 (2006) 388.
[9] W.J. Lu, B.C. Zhao, R. Ang, W.H. Song, J.J. Du, Y.P. Sun, Solid State Communications 136 (2005) 196.
[10] W.J. Lu, B.C. Zhao, R. Ang, W.H. Song, J.J. Du, Y.P. Sun, Physics Letters A 346 (2005) 321.
[11] S. Hashimoto, H. Iwahara, Journal of Electroceramics 4 (2000) 225.
[12] S. Hashimoto, H. Iwahara, Materials Research Bulletin 35 (2000) 2253.
[13] M.A. Carpenter, C.J. Howard, B.J. Kennedy, K.S. Knight, Physical Review B 72 (2005) 024118.
[14] C.J. Howard, B.J. Kennedy, B.C. Chakoumakos, Journal of Physics—Condensed Matter 12 (2000) 349.
[15] B.J. Kennedy, C.J. Howard, G.J. Thorogood, J.R. Hester, Journal of Solid State Chemistry 161 (2001) 106.
[16] B.J. Kennedy, B.A. Hunter, J.R. Hester, Physical Review B 65 (2002) 224103.
[17] C.J. Ball, B.D. Begg, D.J. Cookson, G.J. Thorogood, E.R. Vance, Journal of Solid State Chemistry 139 (1998) 238.
[18] B.J. Kennedy, T. Vogt, C.D. Martin, J.B. Parise, J.A. Hriljac, Chemistry of Materials 14 (2002) 2644.
[19] R.D. Shannon, Acta Crystallographica Section A 32 (1976) 751.
[20] T.M. Sabine, B.J. Kennedy, R.F. Garrett, G.J. Foran, D.J. Cookson, Journal of Applied Crystallography 28 (1995) 513.
[21] B. Hunter, C. Howard, in: A Computer Program for Rietveld Analysis of X-ray and Neutron Powder Diffraction Patterns, Lucas Heights Research Laboratories, Sydney, 1998, p. 1.
[22] M.R. Antonio, J.S. Xue, L. Soderholm, Journal of Alloys and Compounds 207 (1994) 444.
[23] C.S. Wright, R.I. Walton, D. Thompsett, J. Fisher, Inorganic Chemistry 43 (2004) 2189.
[24] Q.D. Zhou, B.J. Kennedy, Journal of Physics and Chemistry of Solids 67 (2006) 1595.
[25] A.M. Glazer, Acta Crystallographica Section B—Structural Science 28 (1972) 3384.
[26] R. Ganguly, M. Hervieu, A. Maignan, C. Martin, B. Raveau, Journal of Physics—Condensed Matter 14 (2002) 9039.
[27] Q.D. Zhou, B.J. Kennedy, C.J. Howard, M.M. Elcombe, A.J. Studer, Chemistry of Materials 17 (2005) 5357.
[28] C. Martin, A. Maignan, M. Hervieu, S. Hebert, A. Kurbakov, G. Andre, F. Bouree-Vigneron, J.M. Broto, H. Rakoto, B. Raquet, Physical Review B 77 (2008) 054402.
[29] O. Chmaissem, B. Dabrowski, S. Kolesnik, J. Mais, D.E. Brown, R. Kruk, P. Prior, B. Pyles, J.D. Jorgensen, Physical Review B 64 (2001) 134412.
[30] C.J. Howard, H.T. Stokes, Acta Crystallographica Section B—Structural Science 54 (1998) 782.
[31] Q.D. Zhou, B.J. Kennedy, Journal of Solid State Chemistry 179 (2006) 3568.
[32] F. Damay, C. Martin, A. Maignan, M. Hervieu, B. Raveau, Z. Jirak, C. Andre, F. Bouree, Chemistry of Materials 11 (1999) 536.
[33] B.J. Kennedy, C.J. Howard, B.C. Chakoumakos, Journal of Physics—Condensed Matter 11 (1999) 1479.
[34] M. Cheah, P.J. Saines, B.J. Kennedy, Journal of Solid State Chemistry 179 (2006) 1775.
[35] B.J. Kennedy, Q.D. Zhou, Solid State Communications 147 (2008) 208.
[36] G. Shirane, Y. Yamada, Physical Review 177 (1969) 858.
[37] B.J. Kennedy, C.J. Howard, B.C. Chakoumakos, Physical Review B 59 (1999) 4023.